Electronic Supplementary Information for

Remarkable high-temperature Li-storage performance of few-layer graphene-anchored Fe_3O_4 nanocomposites as an anode

Mingbao Huang,[a,b] Caihong Chen,[a,*] Songping Wu[a,b,*] and Xiaodong Tian[a,b]

a- *School of Chemistry and Chemical Engineering, South China University of Technology, Guangzhou, 510641, China.*

b- *Guangdong Key Laboratory of Fuel Cell Technology, Guangzhou, 510641, China.*

*Corresponding author. Fax&Tel: +86 -20- 87112897.

E-mail: chchchen@scut.edu.cn (Chen); chwsp@scut.edu.cn (Wu).

Crystal phase and microstructure for product without annealing

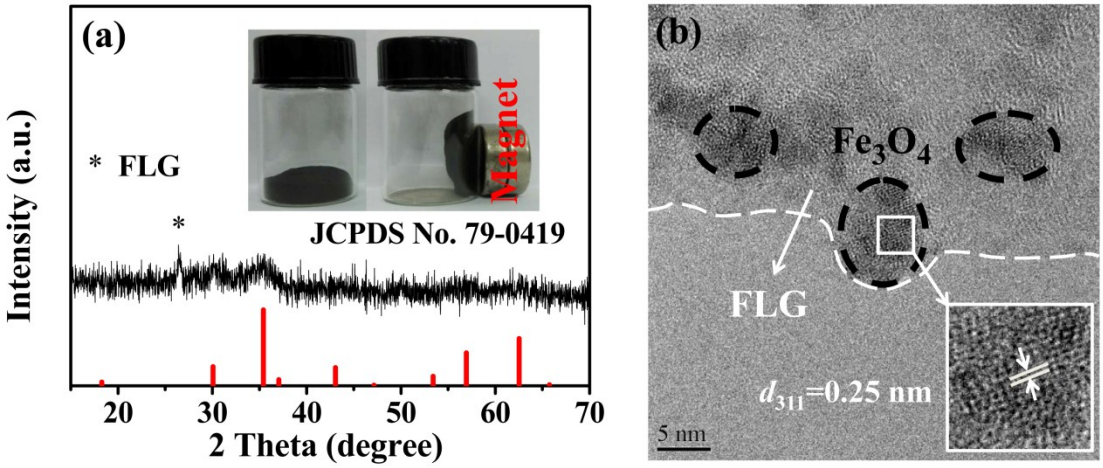

Figure S1. (a) XRD pattern and (b) TEM image of FLG-anchored Fe_3O_4 nanocomposites without experiencing annealing treatment. The magnetic inspection was shown in the inset of (a).

XRD diffraction peaks are unobvious due to poor crystallinity, which also can be corroborated by crystal lattices in the TEM image (**Figure S1b**). A weak peak at 26° represents for specific diffraction of few-layer graphene. The materials show strong ferromagnetic property because the particles can be easily attracted to wall of small bottle by magnets (inset in **Figure S1a**).

XRD patterns

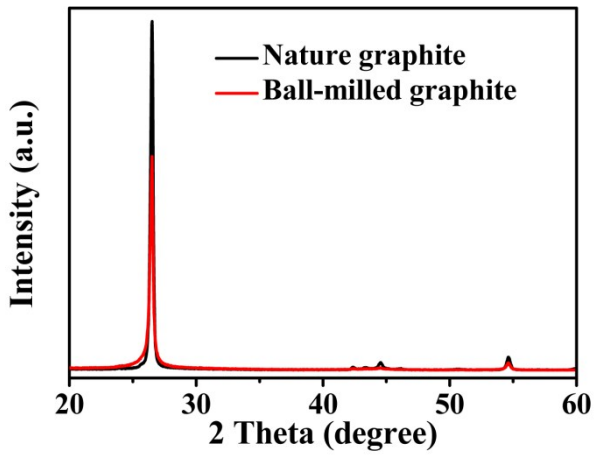

Figure S2. The XRD profiles of nature graphite and ball-milled graphite obtained at a similar condition without K_2FeO_4.

FTIR spectra

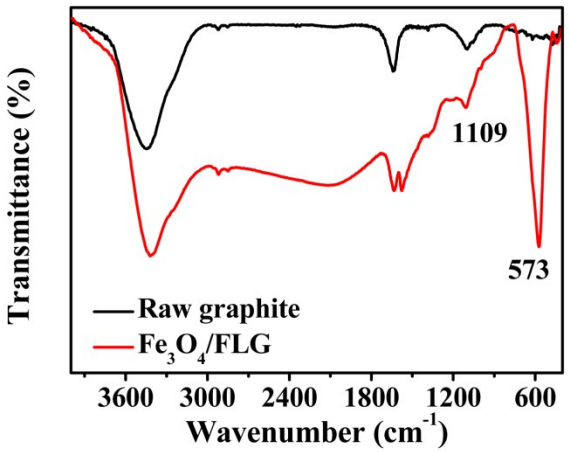

Figure S3. FTIR spectra of FLG-anchored Fe_3O_4 (Fe_3O_4/FLG) nanocomposites and raw graphite.

A strong and sharp peak at 573 cm^{-1} appeared in FTIR spectrum of FLG-anchored Fe_3O_4 nanocomposites, ascribed to the stretching vibration of Fe-O bond.[1] The C-O stretching at 1109 cm^{-1} was detected in the raw graphite, and which presented in the final product with quite intensity. Compared with the spectrum of raw graphite, FLG-anchored Fe_3O_4 nanocomposites don't show different peaks except for the peak of Fe-O.

TEM and SEM images

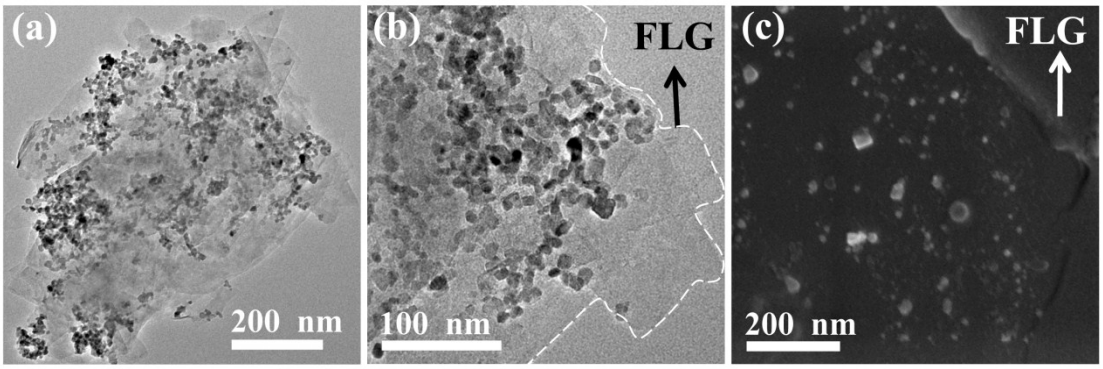

Figure S4. (a), (b) TEM images and (c) SEM image of FLG-anchored Fe_3O_4 nanocomposites.

BET test

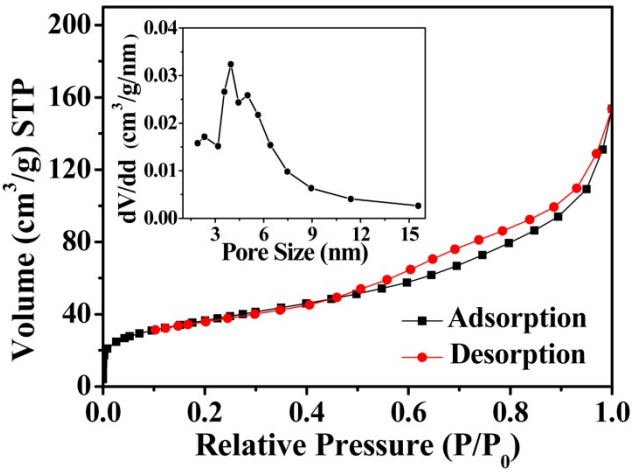

Figure S5. N_2 adsorption/desorption isotherms of FLG-anchored Fe_3O_4 nanocomposites. Pore size distribution was shown in the inset.

TG analysis

In **Figure S6**, loss weight of 1.5 wt% around 100 °C responded to absorbed water, and increased weight of 2.5 wt% from 200 to 400 °C responded to the oxidation process of Fe_3O_4 to Fe_2O_3. Subsequently, weight loss could be ascribed to oxidation of FLG. According to the formula: (23.75 + 2.5) / (100 – 1.5) %, the content of FLG can be calculated to be 26.6%.

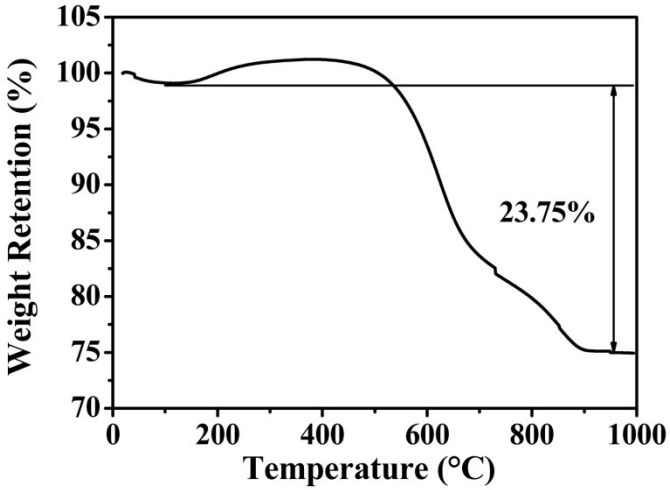

Figure S6. Thermogravimetric result of FLG-anchored Fe_3O_4 nanocomposites.

Capacity contribution of FLG

Firstly, as-prepared FLG-anchored Fe_3O_4 nanomaterials were handled with acid for 5 hours to remove the Fe_3O_4 species, and then washed for several times with distilled water and dried to obtain bare FLG. The FLG was used as anode material to measure its capacity contribution, as shown in **Figure S7**.

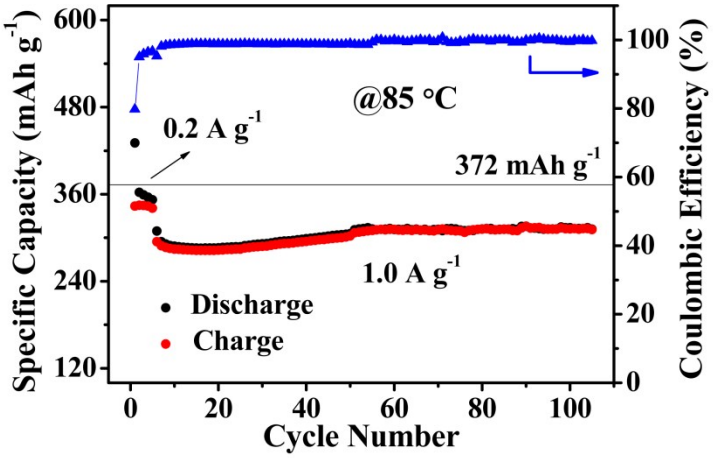

Figure S7. Electrochemical performance of as-obtained FLG with a current density of 0.2 A g^{-1} for first five cycles and 1.0 A g^{-1} for subsequent 100 cycles under 85 °C, and corresponding coulombic efficiency.

FLG exhibited a discharge capacity ~ 357 mAh g^{-1} during the first five cycles. Subsequently, FLG could afford a reversible capacity of 312 mAh g^{-1} after 100 cycles when operated at a current density of 1.0 A g^{-1}. Under the high temperature, the as-obtained FLG has shown good rate performance and excellent cycling stability, with

approaching 100% retention rate of capacity. The average coulombic efficiency was about 98.8%.

Here, the total lithium-storage capacity of the whole composite was composed of capacity of FLG and capacity of Fe_3O_4 according to **Eq.S1**:

$$\text{Total capacity}_{(\text{Composite})} = \text{Capacity}_{(\text{FLG})} \times \text{Content}_{(\text{FLG})} + \text{Capacity}_{(\text{Fe3O4})} \times \text{Content}_{(\text{Fe3O4})} \quad \textbf{Eq.S1}$$

The mass content of FLG was measured as 26.6% by TG analysis in **Figure S6**. At 105th cycle, the discharge capacity of FLG-anchored Fe_3O_4 nanocomposites was 1413 mAh g^{-1} (**Figure 5a**). Therefore, the capacity contribution of FLG toward total capacity could be calculated as follow:

$$\text{Contribution rate} = [\text{Capacity}_{(\text{FLG})} \times \text{Content}_{(\text{FLG})} / \text{Total capacity}_{(\text{Composite})}] \times 100\%$$

$$= [312 \times 26.6\% / 1413] \times 100\% = 5.9\%$$

Electrochemical performance tests at room temperature

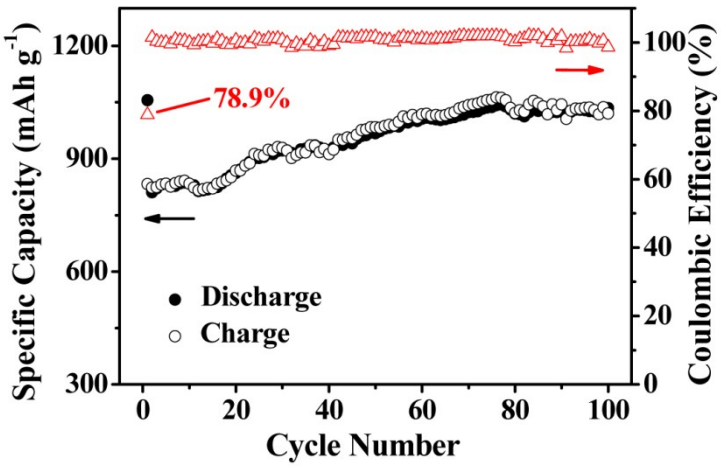

Figure S8. Cycling performance and coulombic efficiency of FLG-anchored Fe_3O_4 nanocomposites at a current density of 200 mA g^{-1} at room temperature.

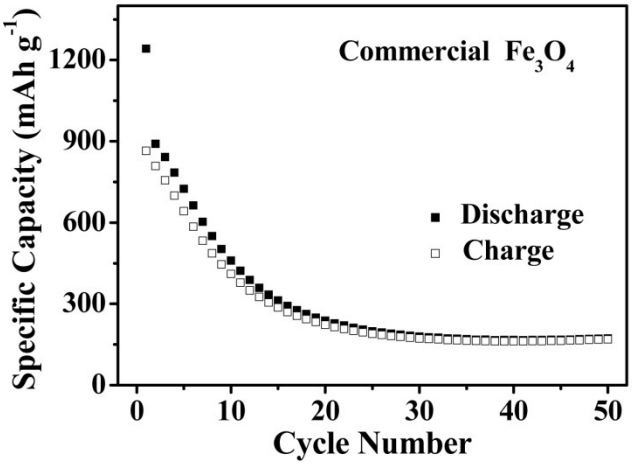

Figure S9. Cycling performance of commercial Fe_3O_4 electrode at a current density of 200 mA g^{-1}.

The initial discharge/charge capacity were measured as 1055/832 mAh g^{-1} (**Figure S8**), with a high initial coulombic efficiency (CE) of 78.9% as compared with that in previous works (less than 70%). [2-4] The initial CE plays a very crucial factor, which determines irreversible degree of lithiation/delithiation reaction. About 21% capacity loss for the first cycle can be attributed to the formation of solid electrolyte interphase layer and irreversible lithiation process. The CE immediately reached approaching 100% at 2nd cycle, suggesting that stable SEI films have been molded during the first cycle. In the early stage of cycling (1 – 15 cycles), profile of reversible capacity was fairly stable due to strong two-dimensional anchoring structure, whereby we believed that the electrode materials were being gradually activated within the stage. After that, capacity of FLG-anchored Fe_3O_4 nanocomposites experienced a visible ascending stage, up to a reversible capacity of 1034 mAh g^{-1} after 100 cycles, with average CE of 99.9% and capacity retention rate of 124%. As a sharp contrast, commercial Fe_3O_4 afforded rapid decay of capacity from a high initial capacity of 1242 mAh g^{-1}, with capacity retention of only 13.6% after 50 charge/discharge cycles (**Figure S9**).

Rate capability

In **Figure S10**, FLG-anchored Fe_3O_4 nanocomposites delivered the specific capacities of 1059, 947, 847, 756, 673, 595, 542 mAh g^{-1} at current densities of 100, 200, 400, 600, 800, 1000, 1200 mA g^{-1}, respectively. The reversible capacity of this material could still return to 1029 mAh g^{-1} when current density decreased to 100 mA g^{-1}, illustrating that this electrode material could maintain its structured integrity, dispelling obvious structural collapse after experiencing a large current impact. While

commercial Fe_3O_4 electrodes merely afforded the capacities of 658, 462, 328, 221, 166, 131, 110 mAh g^{-1}, respectively, and could not achieve effective recovery of capacity.

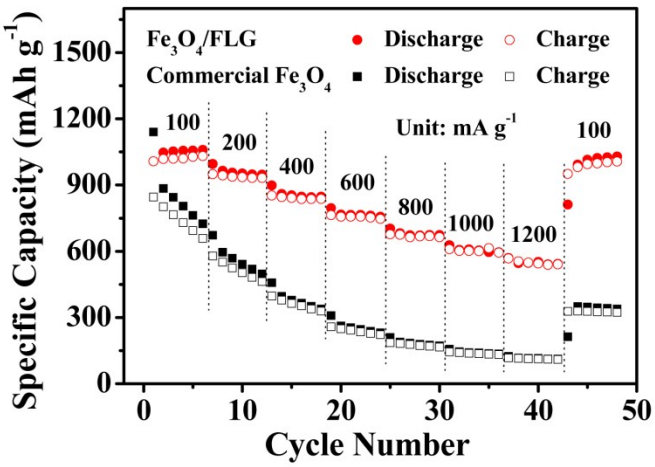

Figure S10. Rate performances of FLG-anchored Fe_3O_4 (Fe_3O_4/FLG) nanocomposites and commercial Fe_3O_4 under different current densities from 100 to 1200 mA g^{-1}.

EIS measurements

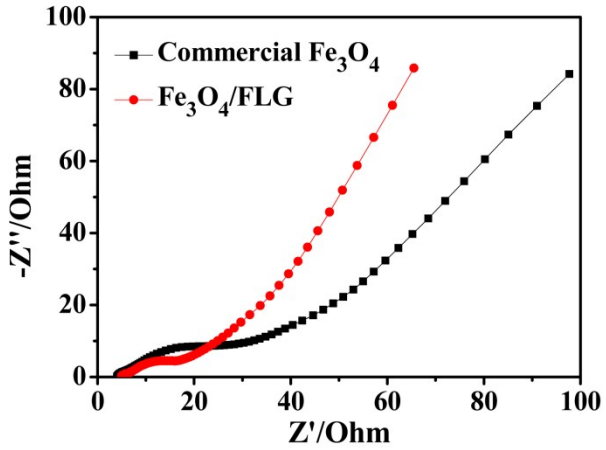

Figure S11. Nyquist plots of FLG-anchored Fe_3O_4 (Fe_3O_4/FLG) nanocomposites and commercial Fe_3O_4 electrodes after the first discharge/charge cycle.

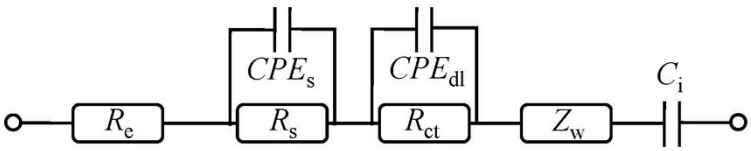

Figure S12. The equivalent circuit diagram of simulating FLG-anchored Fe_3O_4 nanocomposites and commercial Fe_3O_4 electrodes assembled in coin cells. (R_e: electrolyte resistance, R_s: SEI layer resistance, R_{ct}: charge transfer resistance, CPE_s: surface films capacitance, CPE_{dl}: double-layer capacitance, Z_w: Warburg impedance, C_i: intercalation capacitance.)

Table S1. Kinetic parameters of FLG-anchored Fe_3O_4 nanocomposites and commercial Fe_3O_4 electrodes, respectively.

Sample	R_e (Ω)	R_s (Ω)	R_{ct} (Ω)
FLG-anchored Fe_3O_4	5.257	1.921	6.792
Commercial Fe_3O_4	4.388	3.573	15.52

By means of electrochemical impedance spectroscopy, influence of kinetic process for FLG-anchored Fe_3O_4 nanocomposites and commercial Fe_3O_4 electrodes on performance of half-cells were deeply explored (**Figure S11**). Based on the equivalent circuit (**Figure S12**), FLG-anchored Fe_3O_4 nanocomposites possessed a smaller R_s (1.92 Ω) and R_{ct} (6.8 Ω) (**Table S1**), indicating that two-dimensional nanostructure was helpful to accelerate charge transfer between active material and electrolyte. An inclined line at the low frequency region was related to Warburg impedance. Larger slope for FLG-anchored Fe_3O_4 nanocomposites suggested that faster lithium ions diffusion process in electrode materials. [5] Above results could be underlying causes of improved electrochemical performance.

Electrochemical performance test at low temperature

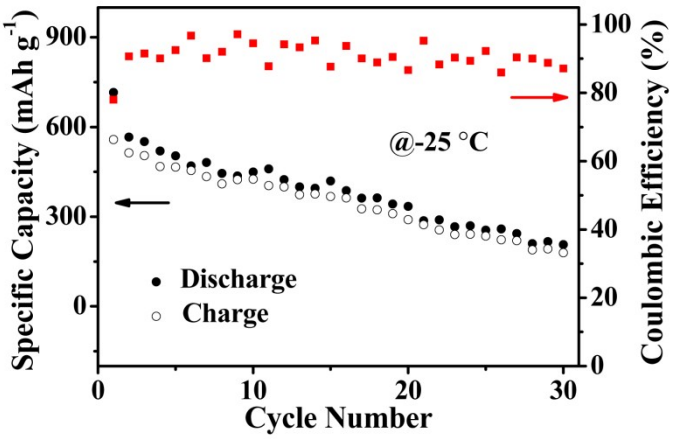

Figure S13. Cycling performance and coulombic efficiency of FLG-anchored Fe_3O_4 nanocomposites with a current density of 100 mA g^{-1} at -25 °C.

To further realize their environmental adaptability, electrochemical response feature of FLG-anchored Fe_3O_4 nanocomposites under a low temperature of -25 °C was discussed, rendering a first discharge capacity of 715 mAh g^{-1} at a current density of 100 mA g^{-1}, with a high initial coulombic efficiency ~ 77.9% (**Figure S13**), following with considerable retention capacity (207 mAh g^{-1}) after 30 cycles. The average coulombic efficiency was 90.6%, less than that at room temperature, which may result from poor lithium ions diffusion and transfer under low temperature. Therefore, such an electrode could be operated at low temperature in spite of sluggish kinetic course. [6, 7]

Electrochemical performances under changeable temperature

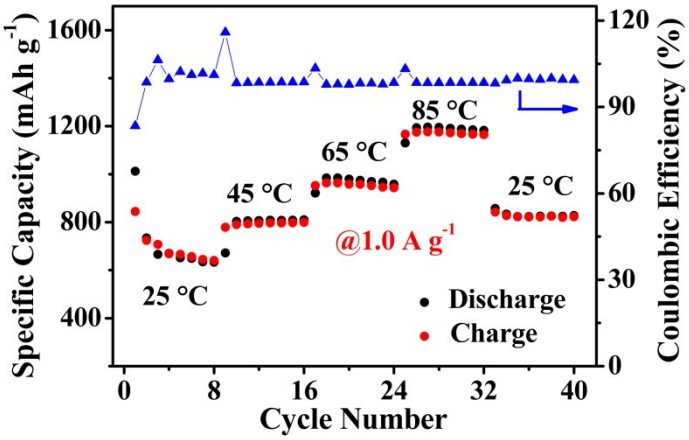

Figure S14. Corresponding electrochemical performances of FLG-anchored Fe_3O_4 under different temperatures with a current density of 1.0 A g^{-1}.

As shown in **Figure S14**, detailed researches about environmental adaptability of this material were carried out by altering operational temperatures at a current density of 1.0 A g^{-1}. Very clearly, the specific capacities of battery gradually increased with temperature increasing. The corresponding discharge capacities were measured as 634, 808, 966 and 1184 mAh g^{-1} at different temperatures of 25, 45, 65 and 85 °C, respectively. As expected, a satisfactory capacity ~ 823 mAh g^{-1} was obtained when operational temperature returned to room temperature, which fully revealed that few-layer graphene-anchored Fe_3O_4 nanocomposites could be successfully operated under ever-changeable temperature.

Table S2. Physical properties and electrochemical performances of iron oxide-based anode materials

Morphology	Synthesis method	Carbon content (%)	Current rate (mA g^{-1})	Temper-ature (°C)	Cycle number	Capacity (mAh g^{-1})	Retention rate (%)	Ref.
Graphene-Fe_3O_4	Hydrothermal method	8	200	25	60	637	58	8
Hierarchical hollow Fe_3O_4	Thermal decomposition	0	1000	25	50	851.9	93	9
Fe_3O_4@rGO	Hydrothermal method	/	1000	25	250	1260	102	10
G/Fe_3O_4@C	Hydrothermal method	28.7	2000	25	200	734	/	1
Graphene-wrapped Fe_3O_4-graphene nanoribbons	Na/K reduction and O_2 oxidization	40	400	25	300	708	89	11
FeO_x@C	Hydrothermal method / etching	14	200	25	100	790	97	4
Fe_3O_4 nanorods/N-doped graphene	Hydrothermal process / annealing	15	100	25	50	929	115	3
Fe_3O_4/C	Ball milling / carbothermal reduction	70	100	25	100	432	95	12
Boron-containing iron oxide	Ball milling / dynamically heating	/	100	25	200	1148	109	13
FLG-anchored Fe_3O_4 nanocomposites	**Ball milling followed by mild annealing**	**26.6**	**200**	**25**	**100**	**1034**	**124**	**This work**
			1000	**25**	**100**	**621**	**95 (after 10th)**	
			1000	**85**	**100**	**1413**	**126**	
			5000	**85**	**100**	**768**	**89**	
			100	**-25**	**30**	**207**	**38**	

CV profiles at room temperature

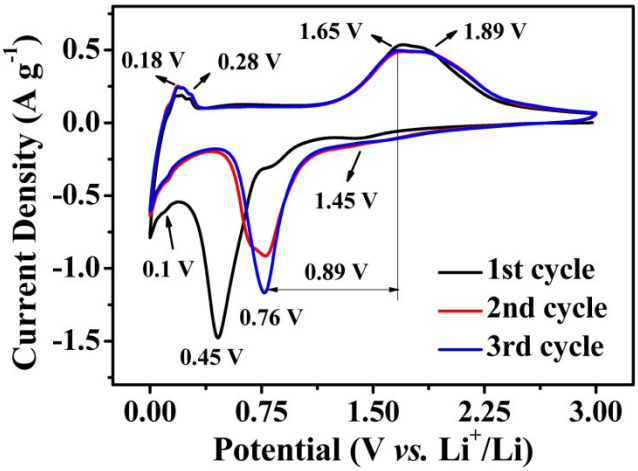

Figure S15. Cyclic voltammetry curves of FLG-anchored Fe_3O_4 nanocomposites with a scanning rate of 0.5 mV s^{-1} at room temperature.

SAED pattern

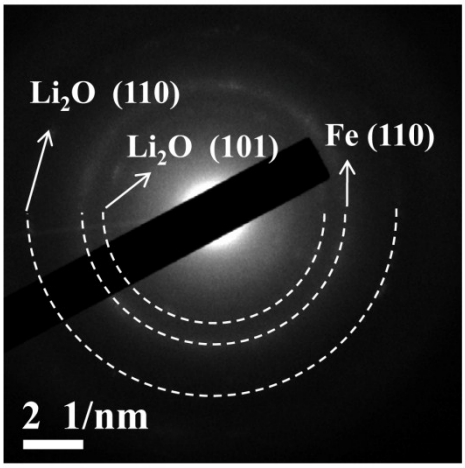

Figure S16. Corresponding SAED pattern recorded on the region of Figure 7(b).

References:

1. X. Jiang, X. L. Yang, Y. H. Zhu, Y. F. Yao, P. Zhao and C. Z. Li, *J. Mater. Chem. A*, 2015, **3**, 2361-2369.
2. W. Zhang, X. Li, J. Liang, K. Tang, Y. Zhu and Y. Qian, *Nanoscale*, 2016, **8**, 4733-4741.
3. J. Jiao, W. Qiu, J. Tang, L. Chen and L. Jing, *Nano Res.*, 2016, **9**, 1256-1266.
4. H. Zhang, L. Zhou, O. Noonan, D. J. Martin, A. K. Whittaker and C. Yu, *Adv. Funct. Mater.*, 2014, **24**, 4337-4342.
5. Y. Jiang, D. Zhang, Y. Li, T. Yuan, N. Bahlawane, C. Liang, W. Sun, Y. Lu and M. Yan, *Nano Energy*, 2014, **4**, 23-30.
6. J.-Q. Huang, X.-F. Liu, Q. Zhang, C.-M. Chen, M.-Q. Zhao, S.-M. Zhang, W. Zhu, W.-Z. Qian and F. Wei, *Nano Energy*, 2013, **2**, 314-321.

7. A. Senyshyn, M. J. Mühlbauer, O. Dolotko and H. Ehrenberg, *J. Power Sources*, 2015, **282**, 235-240.
8. J. Su, M. Cao, L. Ren and C. Hu, *J. Phys. Chem. C*, 2011, **115**, 14469-14477.
9. Q. Q. Xiong, J. P. Tu, Y. Lu, J. Chen, Y. X. Yu, Y. Q. Qiao, X. L. Wang and C. D. Gu, *J. Phys. Chem. C*, 2012, **116**, 6495-6502.
10. Y. Jiang, Z. Jiang, L. Yang, S. Cheng and M. Liu, *J. Mater. Chem. A*, 2015, **3**, 11847-11856.
11. L. Li, A. Kovalchuk, H. Fei, Z. Peng, Y. Li, N. D. Kim, C. Xiang, Y. Yang, G. Ruan and J. M. Tour, *Adv. Energy Mater.*, 2015, **5**, 1500171.
12. P. Wang, M. Gao, H. Pan, J. Zhang, C. Liang, J. Wang, P. Zhou and Y. Liu, *J. Power Sources*, 2013, **239**, 466-474.
13. Y. Cao, Y. Yang, Z. Ren, N. Jian, M. Gao, Y. Wu, M. Zhu, F. Pan, Y. Liu and H. Pan, *Adv. Funct. Mater.*, 2017, **27**, 1700342.